International Journal of Material Forming (2020) 13:393–408
https://doi.org/10.1007/s12289-019-01530-2

ORIGINAL RESEARCH

Experimental studies into the role of cyclic bending during stretching of dual-phase steel sheets

Camille M. Poulin[1] · Sven C. Vogel[2] · Yannis P. Korkolis[3] · Brad L. Kinsey[1] · Marko Knezevic[1]

Received: 5 August 2019 / Accepted: 10 December 2019 / Published online: 3 January 2020

Abstract

Continuous-bending-under-tension (CBT) has been conceived as a mechanical test or a forming process imparting cyclic bending during stretching of a metallic sheet or strip in order to increase its elongation to fracture (ETF) relative to simple tension (ST). In a recent work, over five times improved ETF by CBT over ST has been reported for a dual-phase (DP) steel DP 1180. This paper evaluates the behavior in CBT of three additional automotive advanced high strength steels (AHSS), DP 590, DP 780, and DP 980. In doing so, the process parameter space defined in terms of crosshead velocity applying the tensile force, and roller depth imposing the amount of bending to the specimen has been explored to maximize the ETF of these materials. The studied steel sheets had different thicknesses, in addition to intrinsically containing different fractions of ferrite and martensite phases. After establishing the optimal process parameters, significant improvements in ETF are achieved for all studied steels. Based on comprehensive data, it is found that lower martensitic content moderately improves ETF, while increasing of the sheet thickness rapidly deteriorates ETF, under CBT. The behavior in tension of sheets that were subjected to CBT processing under the established optimal process condition is investigated to determine enhancement in strength and any residual ductility of the materials. In addition to testing, a combination of electron microscopy along with electron-backscattered diffraction and neutron diffraction is employed in order to assess the initial microstructure, evolution of crystallographic texture, and fracture mechanisms for the studied steels. Texture evolution in CBT forms a more pronounced {011} fiber along the stretching direction than in ST, revealing that the deformation in CBT could extend to greater strain levels than those reached at the fracture location in ST. Fractured surfaces after CBT are found to consist of fine ductile dimples, while those after ST consist of coarser dimples and some content of brittle flat martensitic regions.

Keywords Elongation · Plasticity · Fracture · Continuous-bending-under-tension · Advanced high strength steels

Introduction

Much attention in materials science has focused on understanding the relationships between microstructure and response of metals, in terms of strength, work hardening rate, and formability, along with energy absorption during various loading conditions in processing or in service [1–10]. Such understanding is necessary for metals to facilitate optimization of their microstructure and underlying properties for low-cost forming into complex shapes, and then for the necessary structural properties and performances in service. One approach, used with steels, for finding a compromise between strength and ductility, is finding an optimal mixture of different microstructure phases such as martensite and ferrite. Alternatively, for aluminum, the material may be provided in a ductile form for forming, requiring a final aging heat treatment to deliver the required strength by precipitation hardening for service [11–14]. Nevertheless, innovations in sheet metal forming can provide a further strategy to improve materials, e.g. the desired elongation-to-fracture (ETF). To this end, the emphasis can be on discovering forming processes that exploit the ductility throughout the sheet and thus postpone or avoid necking and early fracture.

✉ Marko Knezevic
marko.knezevic@unh.edu

[1] Department of Mechanical Engineering, University of New Hampshire, 33 Academic Way, Kingsbury Hall, W119, Durham, NH 03824, USA

[2] Materials Science and Technology Division, Los Alamos National Laboratory, Los Alamos, NM 87545, USA

[3] Department of Integrated Systems Engineering, The Ohio State University, Columbus, OH 43210, USA

For example, in spin forming, a stationary tool contacts a spinning blank to create an axisymmetric component [15–17]. Another example is a process termed incremental sheet forming (ISF) in which a hemispherical tool locally deforms the sheet imparting plastic strain levels well above those in conventional forming. In both of these processes, only a small portion of the sheet is a plastically deforming zone at each instant. Mechanisms such as shear, bending, nonplanar stress, and cyclic straining have been discussed as origins of the enhanced formability observed in these processes over conventional forming [18]. A theoretical analysis of the effect of shear in sheet forming on increased formability has been presented in [19, 20]. Cyclic straining for boosting formability has been discussed in [21]. The effect of cyclic bending to increase formability has been known for a long time [22, 23]. Moreover, formability in material bending tests can be modified by selection of tool radius or sheet thickness [24]. The beneficial effect of superimposing bending on tension to enhance ETF has also been observed in sheet forming involving draw-beads [25]. Continuous-bending-under-tension (CBT) imparting cyclic bending during stretching of a sheet also achieves strain levels well above those in simple tension (ST) [23, 26, 27].

In this work, we take advantage of the CBT process to evaluate the effect of cyclic bending in stretching of automotive dual-phase (DP) advanced high strength steels (AHSS) steel sheets, DP 590, DP 780, DP 980 and DP 1180. In doing so, the process parameter space defined in terms of crosshead velocity and normalized bend depth imposed onto the specimen has been explored to maximize the ETF for the studied steels. Force vs. displacement curves as a function of these parameters are presented and described. The studied steel sheets had different thicknesses, in addition to intrinsically containing different fractions of ferrite and martensitic phases, allowing us to evaluate both the effect of phase fractions and sheet thicknesses on ETF under CBT. The materials are also tested in ST to establish a reference for assessing the behavior in CBT. The behavior in tension of sheets that were subjected to CBT processing under the established optimal process condition is also investigated to determine enhancement in strength and any residual ductility of the steels. In addition to testing, a combination of scanning electron microscopy (SEM) along with electron-backscattered diffraction (EBSD) and neutron diffraction (ND) is employed in order to assess the initial microstructure, evolution of crystallographic texture, and fracture mechanisms for the studied steels. Comprehensive results from mechanical testing and microstructural characterization along with insights from the analyses of the results are presented and discussed in this paper.

Materials

Premier examples of AHSS are DP steels, four of which are studied in this work. These materials have a composite microstructure made up of martensite islands dispersed in a ferrite matrix. Mechanical behavior of these steels is primarily governed by the volume fraction and distribution of these two phases with their contrasting tradeoff in strength (martensite) and ductility (ferrite) [1, 28–33]. It has been demonstrated that simultaneous improvement of strength and formability of DP steels can be achieved by redistributing the phases [3, 34]. The secondary effects governing the behavior of these steels come from grain size and crystallographic texture per phase. Local plastic deformation of DP steels is highly inhomogeneous due to the grain level inhomogeneities associated with the contrasting phases. Large ferrite grains suitably oriented for crystallographic slip have been observed to deform plastically earlier than small ferrite grains [35]. Strain localizations have been observed within large ferrite grains, ferrite channels between bulky martensite regions, and at martensite/ferrite phase interfaces [29, 35–37]. Such localizations limit ETF during sheet metal forming operations [38–44]. Interestingly, while voids and their coalescence in the ferrite matrix determine ductility of DP steels with low volume fraction of martensite, they do not significantly reduce the overall ductility of DP steels with high volume fraction of martensite. Ductility of high martensite containing steels is more driven by the disparity of properties and interfaces between the two phases [45, 46].

DP steels studied in the present work have been acquired as rolled sheets from US Steel. DP 590, DP 780, and DP 980 are from US Steels' hot dip (HD) processing lines, while DP1180 is from their continuous annealing line (CAL). DP 590 and DP 780 were galvannealed (HDGA) coated, DP 980 was galvanized (HDGI) coated, and DP 1180 was bare. The grades of the commercial DP steel are designated by their ultimate tensile strength (UTS) in MPa. The chemical compositions and treatments are provided in Table 1. The sheet thicknesses were 1.3, 1.4, 1, and 1 mm for DP 590, DP 780, and both DP 980 and DP 1180 respectively. In addition to the effects of martensitic content, these variations allow us to study the effect of thickness on the CBT behavior.

Flow stress

Using an MTS Landmark 370 servo hydraulic loading-frame with MTS 647 hydraulic grips, the as-received sheets were tested in ST at a constant strain rate of 10^{-3} s^{-1} [47–51]. Standard tensile specimens were machined along the rolling direction (RD), 45° from RD, and transverse direction (TD) for DP 980 and DP 1180, while only along RD for DP 590 and DP 780. Dimensions of tensile specimen gauge region were 50.4 mm in length and 11.7 mm in width. The results are shown in Fig. 1. The strain measurements were based on extensometer readings, which were verified using digital image correlation (DIC). At least three samples were tested per category to ensure the accuracy. As is evident, the trend shows an

Table 1 Chemical composition of DP steels (wt%)

	C	Mn	P	S	Si	Cu	Ni	Cr	Mo	Sn	Al	Zr	V	Cb	Ti	B	N_2
DP 590	0.073	1.97	0.014	0.006	0.017	0.04	0.01	0.2	0.172	0.002	0.045		0.001			0.0001	0.005
DP 780	0.1	2.163	0.015	0.006	0.014	0.03	0.01	0.26	0.332	0.003	0.048		0.001	0.003	0.001	0.0001	0.006
DP 980	0.11	2.411	0.013	0.005	0.013	0.027	0.009	0.255	0.385	0.006	0.049	0.005	0.011	0.004	0.002	0.0001	0.0033
DP 1180	0.168	2.222	0.015	0.0053	1.421	0.021	0.007	0.036	0.013	0.007	0.051	0.005	0.012	0.007	0.039	0.0004	0.0086

increase in strength and decrease in ductility from DP 590 to DP 1180. Consistent with our earlier observations [52, 53], the materials show a small amount of anisotropy. Additionally, some dependence on orientation is present for ETF. In the next section, microstructural features governing the behavior of these steels are discussed. The samples exhibited shear localization accompanied with necking followed by fracture, which will also be shown later. The fact that the necking region is severely deformed for every specimen before fracture in ST implies that the material away from the neck has a substantial amount of remaining ductility. Exploiting the ductility of the entire specimen is a motivation for CBT.

Phases, grain structure, and crystallographic texture

Several characterization techniques including SEM with EBSD and ND were used to characterize the initial microstructure of the steels in terms of phase fraction, grain structure, and texture. The SEM-EBSD characterization was performed using a Tescan Lyra3 GMU FIB field emission scanning electron microscope. Samples were manually sanded using SiC papers with 400, 600, 800, and 1200 grit, then polished using water based diamond suspension of 6 μm, 3 μm, and 1 μm on a TriDent PSA cloth, and finally polished to mirror finish using 0.05 μm colloidal silica on a CHEM 2 pad. The mirror finish specimens were etched with 20% Nital for 15 s. Nital was used in order to etch away the ferrite, and leave a topographical surface of martensite. Examples of secondary electron (SE) images for DP 780, DP 980, and DP 1180 are shown in Fig. 2. Image processing of multiple images per material was performed using Matlab to distinguish between martensite and ferrite by color, and calculate an average volume fraction. Average volume fraction of martensite was calculated to be 7.7% for DP 590 [54], 34% for DP 780, 39% for DP 980, and 45% for DP 1180. The phase fractions were also verified for DP 590 and DP 1180 using EBSD image quality (IQ) maps, where regions of martensite appear as dark regions due to scan being indexed as BCC crystal structure, where martensite has BCT crystal structure. Increased amounts of martensite in these steels increases the strength considerably, but also increases their brittleness and decreases their ductility (Fig. 1).

EBSD was performed using an Edax EBSD detector attached to the SEM detailed above. The steels were polished to a mirror finish using the same procedure as for SE imaging, but not etched. Figure 3 shows the inverse pole figure (IPF) maps of the initial structure for all four DP steels. Scan step sizes were 0.1 μm, 0.1 μm, 0.06 μm, and 0.05 μm for DP 590, DP 780, DP 980, and DP 1180, respectively. Different step sizes were used in an effort to differentiate feature sizes, as well as to maximize the size and minimize scan time. All four scans were indexed for ferrite. The data for DP 590 is taken from [54]. The maps feature pockets of martensite in increasing amounts from DP 590 to DP 1180. DP 780 and DP 980 exhibit some gradients in crystal orientation within the grains. Additionally, the ferrite grains in these steels are smaller than in DP 590 and DP 1180. Thus, it is more difficult to differentiate the martensite groups from the ferrite using EBSD. As a result, volume fraction of martensite was difficult to estimate based on confidence index and IQ analysis. Nevertheless, indexing of both ferrite and martensite was very good owing to the high quality of polishing. It is worth mentioning that we have attempted to index martensite as the body-centered tetragonal (BCT) structure hoping to succeed, at least for DP 1180. However, it proved to be very difficult to get a good confidence index, even in large martensite clusters. The BCT

Table 2 Properties based on the flow curves from Fig. 1

	DP 590 (RD)	DP 780 (RD)	DP 980 (RD)	DP 980 (45)	DP 980 (TD)	DP 1180 (RD)	DP 1180 (45)	DP 1180 (TD)
0.2% offset yield stress (MPa)	407	528	630	612	634	839	850	851
UTS (MPa)	663	913	987	958	1012	1194	1198	1223
Eng. strain at UTS	0.146	0.109	0.0808	0.0853	0.0658	0.0619	0.0573	0.0545
Eng. strain at fracture	0.187	0.1318	0.0971	0.105	0.0764	0.0767	0.0686	0.064

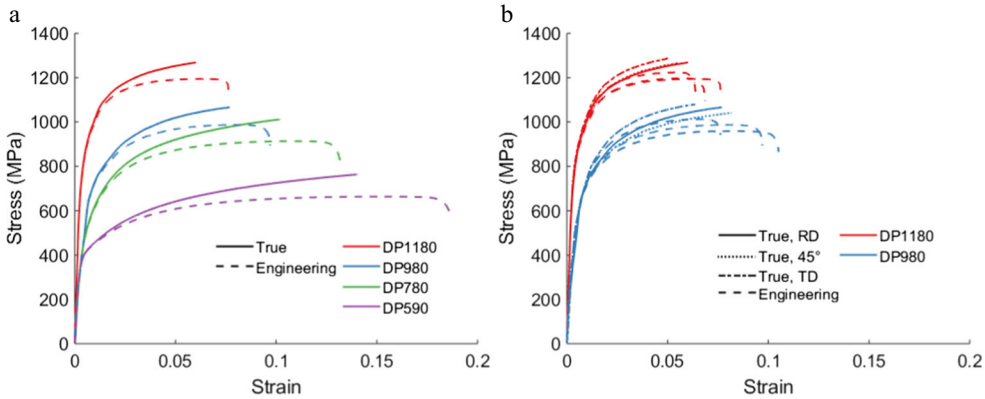

Fig. 1 Engineering (dashed lines) and true (solid lines) stress-strain curves for DP steels along their **a** rolling direction (RD) and **b** RD, transverse direction (TD) and 45° direction from RD/TD in simple tension (ST) under a strain rate of 10^{-3} s^{-1}. Note that the line type differentiates testing directions, while different colors represent materials. Dashed line is consistently used for the "Engineering" curves (Table 2)

crystal structure of martensite is close enough to the body-centered cubic (BCC) structure of ferrite, which indexed to a high confidence index for both ferrite and martensite.

Larger scans of over 100 μm in height and width were taken of the same samples scanned in Fig. 3 in order to get enough statistics for stereographic pole figures to show texture in the steels. The scans consisted of over a million indexable points with high confidence index. Pole figures in Fig. 4 show the initial texture of the four DP steels considering all indictable points, which resemble classically reported orthotropic rolled texture for BCC materials, where the grains are concentrated around the γ-fiber and a portion of the α-fiber [55–62]. Texture evolution during CBT will be presented for DP 1180 in the results section of the paper. These measurements are based on ND, which is a more accurate technique for macroscopic texture characterization [63–67]. Unlike EBSD, ND measures textures averaged over mm^3 to cm^3 volumes due to the deep penetration of thermal neutrons into the materials, combined with beam spot sizes of ~0.1–1 cm^2.

CBT testing

CBT has been established as an experiment capable of significantly increasing ETF in sheet metals [27, 52, 68–70]. The test closely resembles a classical ST test while suppressing the instability that limits ST. During CBT testing, a sheet/strip is pulled in tension and continuously bent/unbent by rollers, which incrementally deforms the material, depleting its ductility throughout, as opposed to localized necking [18, 71–73]. Universal tensile testing machines furnished with a set of moving rollers have been typically used for CBT testing [23, 27]. A specialized CBT machine has been previously presented in [70]. This machine is used in the present work (Fig. 5).

The machine is a horizontal tabletop setup, described in detail in [70]. The other significant contrast to the tensile testing machine for CBT [23, 27] is that the specimen passes through the rollers rather than the rollers passing over the specimen. The main benefit of stationary rollers is that as the length of the specimen increases with the pull of the hydraulic cylinder, the entire gauge section of the specimen is still symmetrically traversed through the rollers, where at the beginning and the end of the cycle the rollers return to the same exact location. This is accomplished by using a mechanical limit switch attached to the grip on the hydraulic cylinder. Thus, the 1x, 2x, and 3x deformation regions remain distinct. The regions would interfere if the rollers would be moving for a constant value of stroke like in the moving rollers machine adaptations [23, 27]. The stationary rollers also allow for easy observations, in real-time, of the process zone around the three rollers. The machine is designed for CBT testing of wide sheets, beyond the strips reported here.

The roller assembly is attached to the base, which is the only stationary component. The three rollers are 25.4 mm in diameter, 200 mm in length. The bottom rollers are spaced 27 mm from the center roller. The two bottom rollers are in a fixed position, and the center top roller is lowered to create bending at a bend depth measured using gauge blocks. The bend depth is defined by the distance from zero that the center roller is lowered, δ. The value is often divided by the material thickness, t (δ/t) to create a normalized value. The carriage, along with the hydraulic cylinder and gripped specimen, cycle back and forth on the base using a ball screw. The speed of the ball screw is a constant 66 mm/s for every experiment, except at the end of each stroke of the carriage, where it stops to reciprocate. The specimen is gripped on the left and right side of the stationary roller setup, each attached to a load cell to measure force. Only the data from one load cell is necessary to report because, with the exception of which direction the carriage is moving, they are reading the same force, but the peak and valley force alternate between maximum and minimum values. The load cell from which all the reported data is taken is a Futek compression load cell with a capacity of 22.4 kN. The grip on the right side of the stationary rollers is attached to

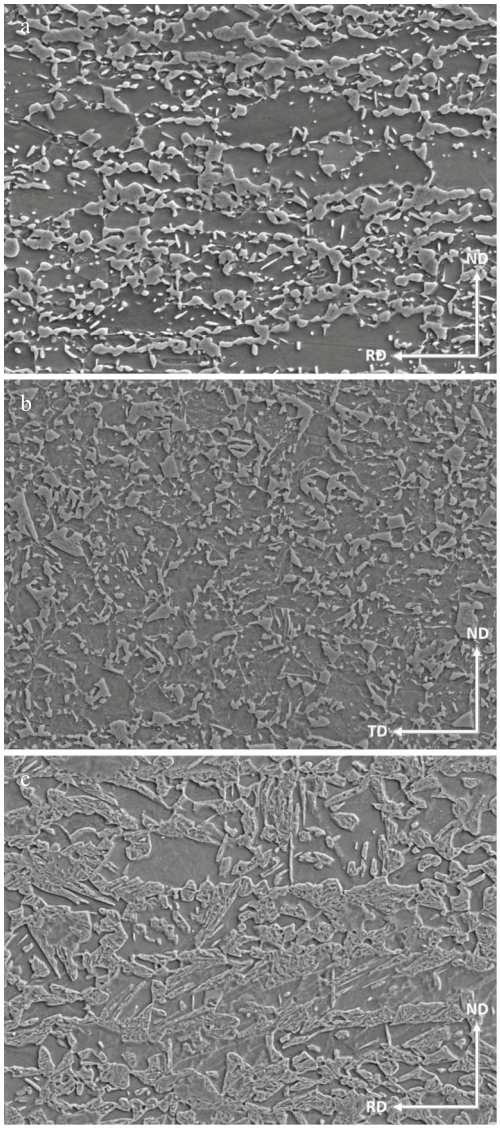

Fig. 2 Secondary electrons (SE) micrographs showing ferrite and martensite in samples of **a** DP 780, **b** DP 980, and **c** DP 1180. View field is 50 μm in width and 40 μm in height for each image. Dark etching areas are ferrite, while the white islands are martensite. Volume fraction of martensite is 7.7% for DP 590 [54], 34% for DP 780, 39% for DP 980, and 45% for DP 1180

a Sheffer hydraulic cylinder with a 310 kN pull force capacity which applies the tension, and a Balluff Micropulse displacement sensor to record displacement of the cylinder crosshead. Two limit switches are used to control the stroke of the carriage. One is a ferromagnetic switch attached to the front of the stationary base, which senses the leading edge of the carriage. The second is a mechanical switch which is triggered by an extrusion from the rear side of the roller assembly. A cycle is defined as two strokes, where the carriage first reaches the opposite side, and then returns back to its original position.

Each test begins with a cycle without tension, only bending. After the first cycle, the hydraulic cylinder introduces tension at a constant crosshead velocity. The test is then continued until the specimen fractures, or the number of cycles in an interrupted test are met. If the CBT process is interrupted after a certain number of cycles, any residual ductility as well as strength of the material can be assessed by secondary tensile tests [26]. The number of CBT cycles reported does not include the first cycle of only bending. In the case of interrupted testing, the number of cycles stated are CBT cycles. Interrupted CBT experiments were performed at the ideal parameters which are defined later, and were ran up to a defined number of cycles (2, 4, 6, 8, 10, and 12). Then the machine was stopped without fracturing the specimen. From this unbroken specimen, subsize specimens are machined using wire EDM.

Each CBT specimen is dog bone shaped, shown in Fig. 6. The gauge section of each CBT specimen is 200 mm in length and 11.7 mm in width. The deformation in the gauge length is defined by three different regions [26, 70]. The specimen is gripped so that these deformation regions are symmetrical across the length of the specimen. The 1x region is only traversed by one roller per cycle, meaning that region is only bent and unbent once per cycle. The 2x region is only traversed by two rollers per cycle, being bent and unbent twice, and similarly the 3x region, being bent and unbent three times per cycle. These regions are important to define in order to concentrate on the area that is undergoing the most deformation (3x region). This region is where the subsize specimens are machined from. The subsize specimens are ASTM E8 with a gauge section 32 mm in length and 6 mm in width. The entirety of the subsize specimen gauge section is machined from the 3x region of the interrupted test specimens. These specimens are pulled in secondary ST at a constant strain rate of 10^{-3} s^{-1} to evaluate their enhancement in strength and residual ductility. The secondary ST experiments were performed on the MTS machine, which is used for the ST experiments of Fig. 1.

Results

Typical force-displacement curves recorded during CBT testing are presented in Fig. 7. The increase in elongation to fracture over ST is evident, as well as the decrease in necessary pull force. The CBT curves are characteristic compared to standard material characterization curves, with a repeating pattern of peaks and valleys. The peaks correspond to the carriage stopping to reverse direction, creating pure tension because the hydraulic cylinder pulls the specimen at a constant rate independent of carriage movement. The valleys correspond to the carriage being at constant velocity within the cycle, where there is both bending and tension. The peaks and valleys have alternating maximums and minimums depending on the stroke of the carriage. If the carriage is moving away from the load cell, the peaks and valleys are at a

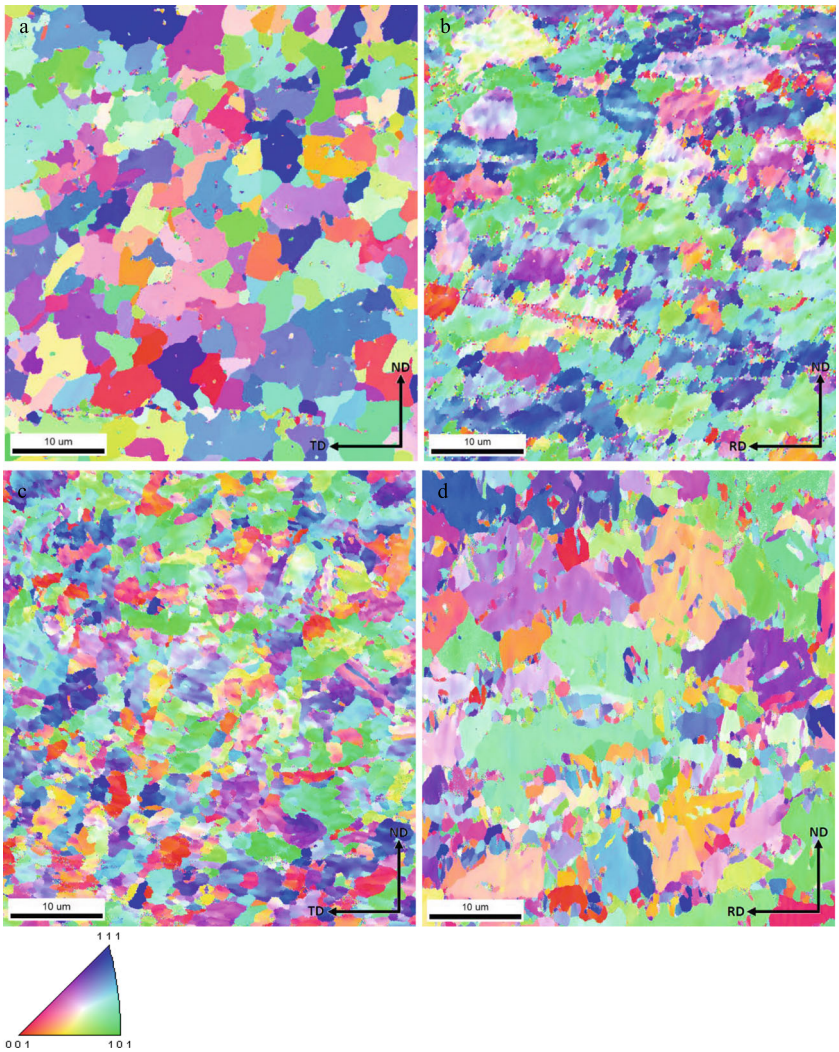

Fig. 3 Inverse pole figure (IPF) maps of the initial microstructure for **a** DP 590, **b** DP 780, **c** DP 980, and **d** DP 1180. The colors in the maps represent the orientation of the sample axis perpendicular to the maps with respect to the local crystal lattice frame according to the IPF triangle. The scale-bar shown in the maps is 10 μm

maximum, and if the carriage is moving toward the load cell, the peaks and valleys are at a minimum [70]. DP 590 and DP 780 show higher forces relative to DP 980 and DP 1180 which is attributed to the higher sheet thickness. In contrast, considering that the addition of bending to the tensile load lowers the force required to reach the plastic flow stress of the material on the outward surface of the strip, thicker sheets require lower forces because of larger bending curvature and resulting stress/strain.

The combination of a bending stress with a tensile force in a CBT setup leads to a non-symmetric stress profile of tension/compression, with the neutral axis cyclically shifting towards the surface of the roller over which the sheet is passing (Fig. 6b, c). The effect is a function of sheet thickness. The CBT processing is conducted at a uniaxial stress level below the yield stress of the material. In addition to the influence of bending, the Bauschinger effect is present due to the reverse loading as a point of the strip moves from bending in tension (with, e.g., a roller above it) to bending in compression (with, e.g., a roller below it) in a cyclic fashion. This also serves to reduce the required load for plastic deformation. As already explained, a higher bend depth requires a lower force for the elongation. At a lower crosshead velocity, the number of bending/unbending operations to obtain a certain elongation is higher, while the observed force is lower. Here, the deforming though-thickness stress profile of the axial stress spanning the gauge section of the specimen is more frequent.

In a recent work, we have carried out CBT on DP 1180 steel [52]. Over five times improved ETF for DP 1180 observed in that work provided a promising means to evaluate the effect of CBT for other AHSS. Similar to the earlier work involving DP 1180, we begin by performing a parameter study to determine the ideal bend depth and crosshead velocity for the highest amount of ETF for DP 980. Three material directions were explored in this parameter study, RD, TD, and 45° from the RD or TD. Five different normalized bend depths and two different crosshead velocities were used in determining the optimal parameters. The normalized bend depths used were 2, 2.5, 2.75, 3.5, and 4.25. The two crosshead velocities used in the parameter study were approximately 1 mm/s, and

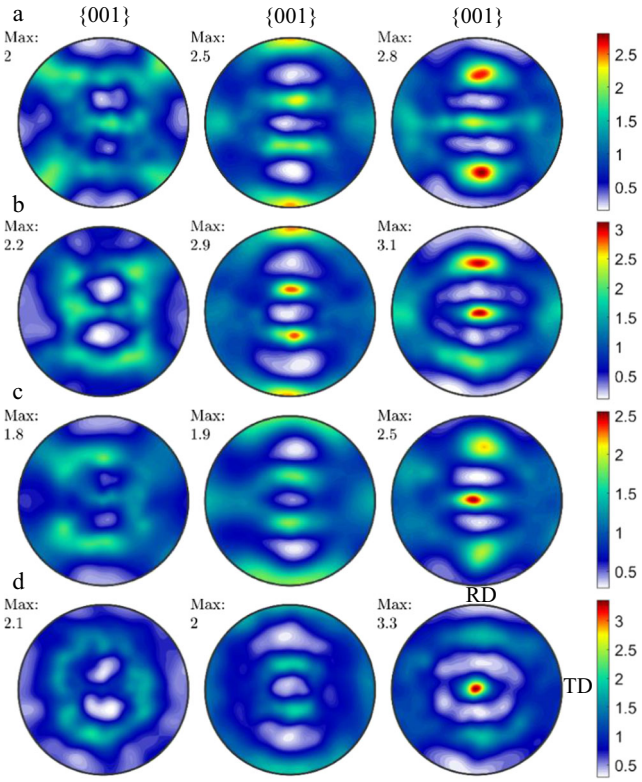

Fig. 4 Stereographic pole figures measured using EBSD showing initial texture in the sheets of **a** DP 590, **b** DP 780, **c** DP 980, and **d** DP 1180

1.35 mm/s. Velocities are approximate values due to the nature of the experimental setup, where the input is a voltage for the hydraulic cylinder, not a specific velocity value. After seeing a decreased benefit at 1.75 for the slower velocity, 2 was the minimum normalized bend depth used at the fastest velocity.

Figure 8 shows the results of the parametric study. The plots on the right show ETF in CBT normalized by ETF in ST to better reveal the significant improvements in ETF relative to ST. The results for DP 1180 are also provided to facilitate the comparisons. In the TD direction, both DP 980 and DP 1180 were tested at 1.2 mm/s crosshead velocity and normalized bend depths of 2.5 and 3.5 for comparison to earlier experiments involving an aluminum alloy, AA6022-T4 [70].

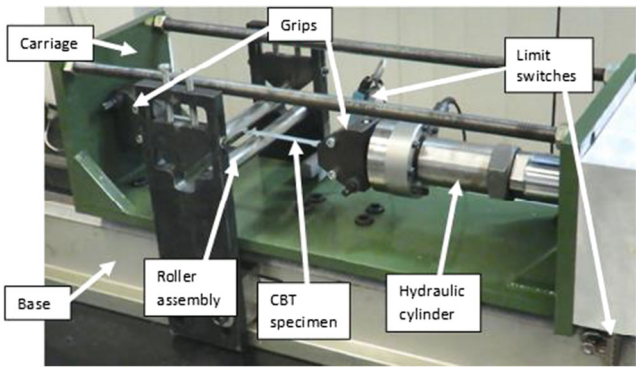

Fig. 5 Main components of the CBT machine

In the majority of cases for all three directions of DP 980, a normalized bend depth of 3.5 and crosshead velocity of 1.35 mm/s were considered to be the ideal parameters for increased elongation to fracture. For these parameters, the material is not under- or over-bent, and thus, more displacement before fracture is possible. If under-bent, the strip/sheet is exposed to ST, primarily. With increasing the crosshead velocity for a fixed amount of bending more of the deformation is caused by ST than bending. Since plastic deformation occurs only in the region underneath the rollers, the amount of the sheet exposed to ST increases as the area of contact between the rollers and the sheet reduces with crosshead velocity. As is evident, with increasing the crosshead velocities up to a certain level, even though there is more ST deformation in the sheet, more displacement before fracture can be achieved. However, there is a limit to the increase in the crosshead velocity and thus ST in the sheet, after which the displacement before fracture would reduce [52]. If over-bent, the introduced bending fields lower the displacement before fracture. Moreover, the effect of friction is more significant when the wrapping around the rollers increases. In summary, ETF improves with the crosshead velocity and with the bending depth up to a certain level, after which it decreases. A faster crosshead velocity of 2 mm/s was explored with DP 1180 [52], but due to minimal increase in elongation to fracture, the slower velocity of 1.35 mm/s was chosen for the ability to run more cycles before fracture which is valuable for interrupted testing. In some cases, DP 980 showed better results at a normalized bend depth of 4.5, but for consistency, a normalized bend depth of 3.5 and crosshead velocity of 1.35 mm/s were chosen as optimal for future interrupted experiments. It should be noted that the observations are based on the discrete tests described here. A rigorous optimization study likely involving a combination of experiments and simulations could arrive at true optimal values for these parameters maximizing ETF. In summary, DP 980 parameter testing proved the same trend as DP 1180 where the faster crosshead velocity along with 3.5 normalized bend depth resulted in a higher elongation to fracture. Moreover, the study revealed even better behavior in CBT of DP 980 than DP 1180, suggesting that lowering the content of martensite from 45% for DP 1180 to 39% for DP 980 is beneficial for ETF in CBT.

The optimal parameters were also used to test DP 590 and DP 780. Three tests were performed to further evaluate the effect of martensite and sheet thickness on the CBT behavior. Both steels were tested at 1.2 mm/s crosshead velocity and normalized bend depths of 2.5 and 3.5 for comparison, and the chosen ideal parameters of 1.35 mm/s crosshead velocity and normalized bend depth of 3.5. DP 590 only fractured in the case of 2.5 normalized bend depth and 1.2 mm/s crosshead velocity due to the limits of the hydraulic cylinder. The results are shown in Figs. 7 and 8. Based on lower content of martensite in DP 780 (34%) relative to DP 980 (39%), one would

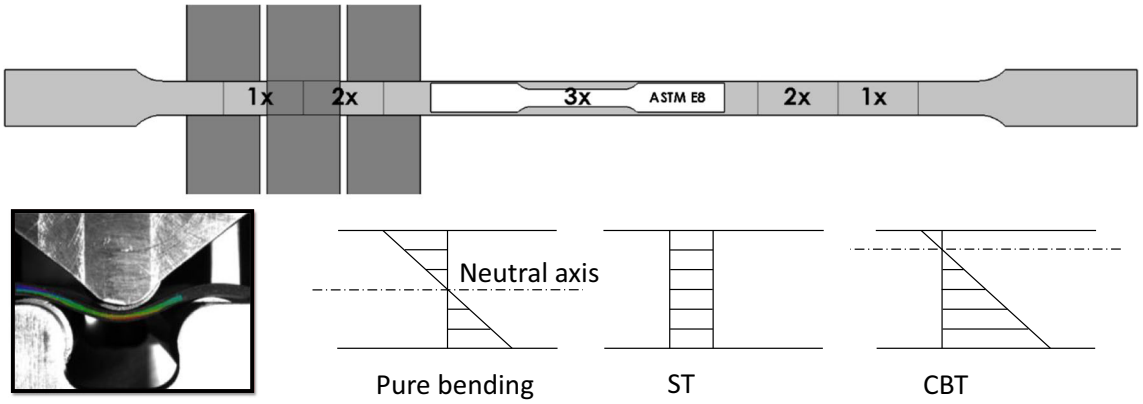

Fig. 6 **a** Schematic of a CBT specimen with a subsize specimen for subsequent ST. The initial CBT specimen has a gauge section length of 200 mm and 11.7 mm width. The subsize specimen has a gauge section length of 32 mm and 6 mm width. The deformation regions, 1×, 2×, and 3×, are indicated, defined by roller location. **b** Photograph showing a side view of the local geometry of the strip during CBT. **c** Schematic of the axial stress/strain state in a strip that is bent in pure bending elastically, stretched in ST, and bent elastically and stretched at the same time underneath the middle roller in CBT. The neutral axis would shift similarly for an elasto-plastic stress/strain state in the strip but the stress/strain profiles would be nonlinear

expect better behavior in CBT. However, the increase in sheet thickness from 1 mm to 1.4 mm has a significant effect deteriorating the CBT behavior. For the final verification of the effects of thickness and martensitic content, we tested DP 590. The expectation is better behavior in CBT relative to DP 780 because of lower content of martensite (7.7%) and reduced thickness to 1.3 mm. The results in Fig. 8 show the expected trend. The two maximum points for DP 590 overlap because the specimens in these tests never fractured before the entire stroke of the hydraulic cylinder was consumed. The true value at fracture for both of these tests would be higher than shown.

Secondary ST testing of the interrupted specimens processed by CBT was performed to explore the enhanced strength and residual ductility of all four AHSS. Additionally, these specimens for DP 1180 were used to study texture evolution during CBT. These CBT tests were run at the chosen ideal parameters of 1.35 mm/s crosshead velocity and 3.5 normalized bend depth. CBT tests were run to a specified number of CBT cycles without fracturing the specimen. Then, the test was stopped. All four steels were run to 2, 4, 6, and 8 CBT cycles, and some up to 10 and 12 CBT cycles, if possible before fracture. ASTM E8 subsize tensile specimens were then machined from the CBT processed specimens and pulled in ST at a strain rate of 10^{-3} s^{-1}. Both DP 590 and DP 780 were tested in the RD direction, and DP 980 and DP 1180 were tested in the RD and TD. Results are shown in Fig. 9. The appendix Table 3 summarizes the material properties extracted from these tests.

All four steels, in all three directions revealed the same trend: increased strength and decreased ductility with the increase in number of CBT cycles. The yield stress and UTS increase with increased number of cycles, and engineering strain at UTS and fracture decrease with increased number of cycles. Another interesting result is the significant amount of necking in each test, observed by the engineering stress strain curves in Fig. 9. ST tests of the initial material have very little necking as seen in Fig. 1, compared to the significant amount of necking in the ST testing of the subsize specimens. The post-uniform elongation does decrease with increased number of CBT cycles, as expected with the decrease

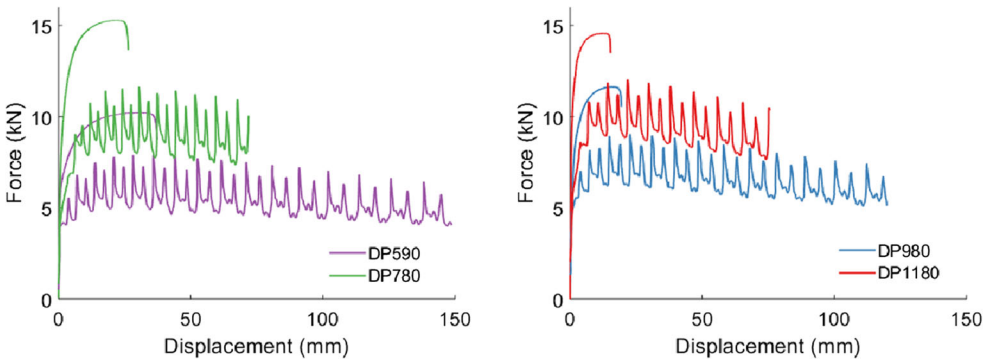

Fig. 7 Typical force-displacement curves during CBT testing (with spikes and plateaus). These curves are recorded during testing under a crosshead velocity of 1.35 mm/s and a normalized bend depth of 3.5 in the RD. The corresponding simple tension curves (with no spikes and plateaus) are shown for reference. The thicknesses of the as-received sheets are 1.3, 1.4, 1 and 1 mm for DP 590, 780, 980 and 1180, respectively. DP 590 curve is not to fracture, but to the limits of the machine

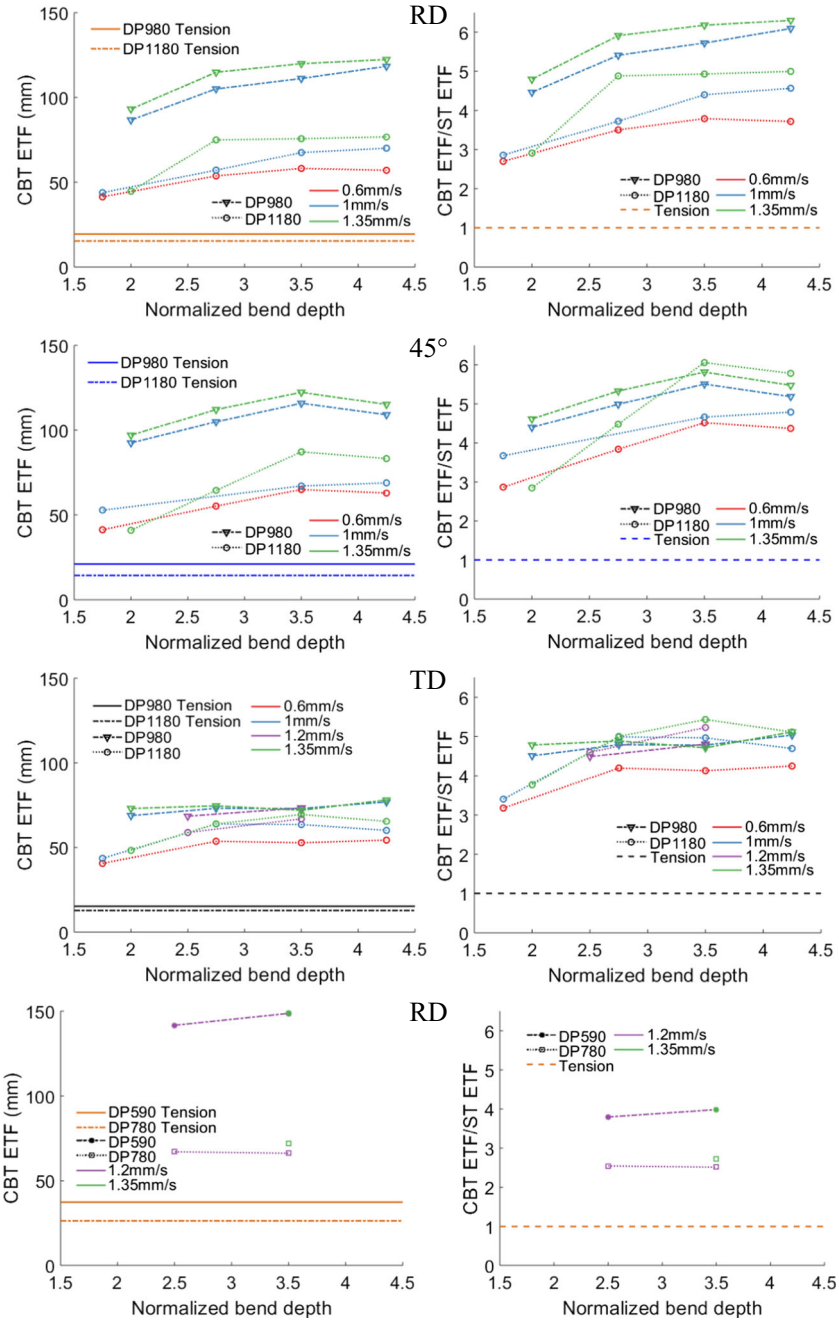

Fig. 8 Elongation-to-fracture (ETF) achieved by CBT testing. Plots normalized by ETF in simple tension are also shown. The arrow indicates that for DP590 the stroke limit of the CBT machine was reached; therefore, fracture did not occur

in ductility. The strengthening is higher for low martensite containing steels, which could be attributed to formation of dislocation substructures in ferrite [74]. Future research will attempt to develop a methodology for inferring post-necking behavior of these steels based on the data presented in Fig. 9.

The interrupted CBT test specimens were also used to study texture evolution in DP 1180 during CBT. ND was conducted on eight different samples using the High Pressure/Preferred Orientation (HIPPO) beam line at the pulsed neutron spallation source at LANSCE, Los Alamos National Laboratory, which is a neutron time-of-flight diffractometer for bulk microstructural characterization of materials at ambient and non-ambient (temperature, pressure, and load) conditions [75]. The eight different samples are: initial material, sample fractured in ST in the fracture zone, sample fractured in ST away from the fracture zone, but within the gauge section, and the 3x region of CBT processed interrupted specimens at 2, 4, 6, and 8 CBT cycles. A 2 mm slit was used to measure texture approximately 2 mm from tips over the entire sample width and thickness. Count time was equivalent to approximately 20 min at a proton current of 100 microA. The

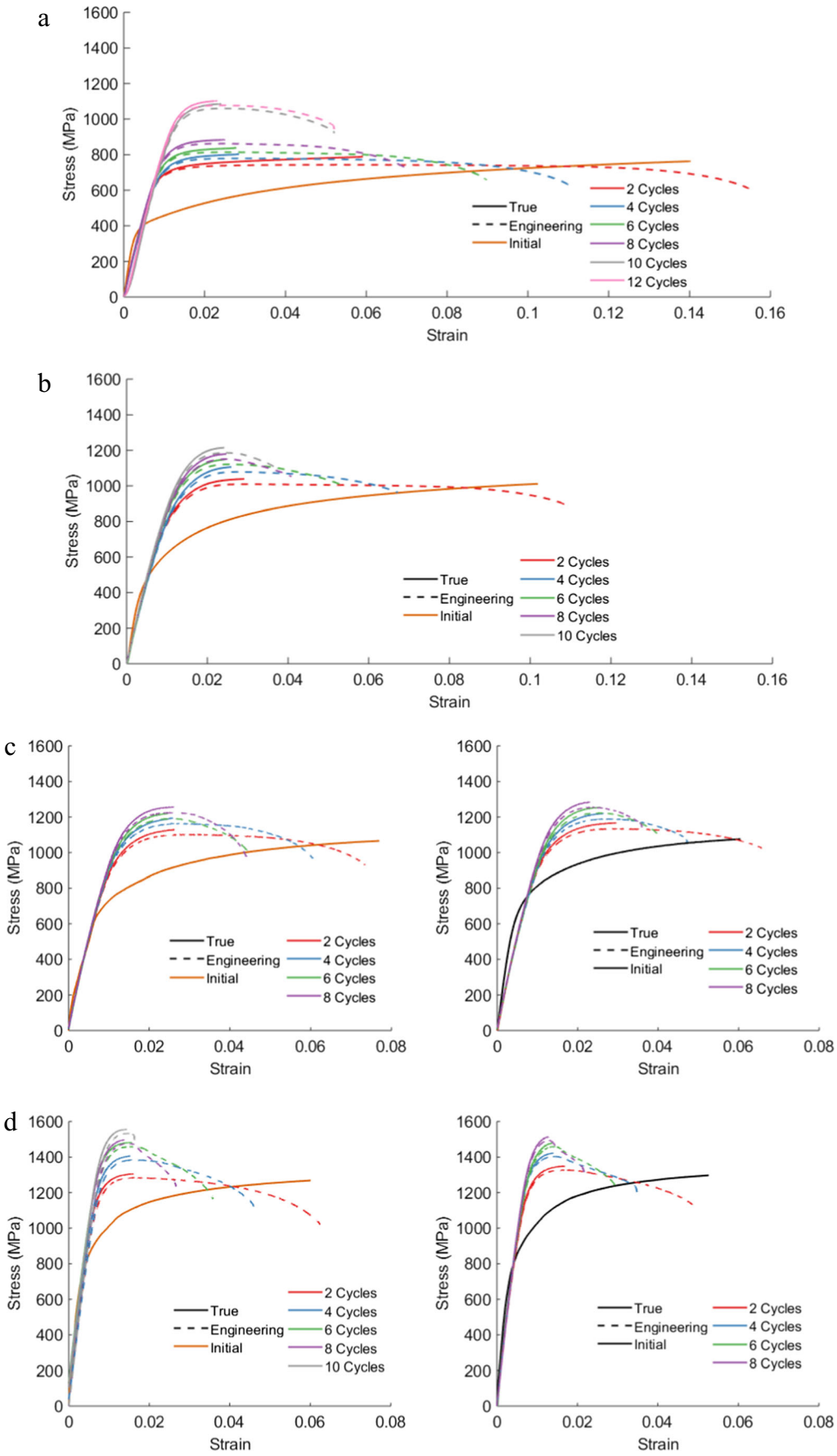
a
Stress (MPa)
Strain
True
Engineering
Initial
2 Cycles
4 Cycles
6 Cycles
8 Cycles
10 Cycles
12 Cycles
b
c
d

◀ **Fig. 9** Engineering (dashed lines) and true (solid lines) stress-strain curves measured under a strain rate of 10^{-3} s^{-1} after interrupting CBT processing at 1.35 mm/s crosshead velocity and 3.5 normalized bend depth to a certain number of CBT cycles indicated in the legends for **a** DP 590 along RD, **b** DP 780 along RD, **c** DP 980 along RD (on the left) and TD (on the right), and **d** DP 1180 along RD (on the left) and TD (on the right)

technique measures many inverse pole figures (i.e. in 135 sample directions) ensuring a sufficient coverage to fit an orientation distribution function (ODF) in a simultaneous Rietveld refinement of 135 patterns, including also structural parameters such as lattice parameters and weight fractions [76]. Rietveld refined ODF is then used to obtain pole figures per sample. Both ferrite and martensite are included in the measurements because their diffraction peaks overlap. The ODF analysis of the data was completed using MAUD [76] with 7.5 degree resolution, while the pole figures are plotted in MTEX [77].

Figure 10 shows measured pole figures of the initial texture and those after ST testing. Similarity between pole figures in Fig. 4 (measured using EBSD) and those in Fig. 10 for the initial texture of DP 1180 indicates that the size of the EBSD scans was sufficient to obtain the texture data. Considering relatively small plastic straining of DP 1180 in ST, texture does not evolve substantially, even in the region at and near the fractured surface. The texture in the deformed samples in ST still resembles rolling texture. Nevertheless, some evidence of {011} pole aligning with loading in the TD direction can be observed. Formation of the {011} fiber texture is expected for BCC metals deformed in ST [56]. The fiber is more pronounced around the fracture zone than away from it

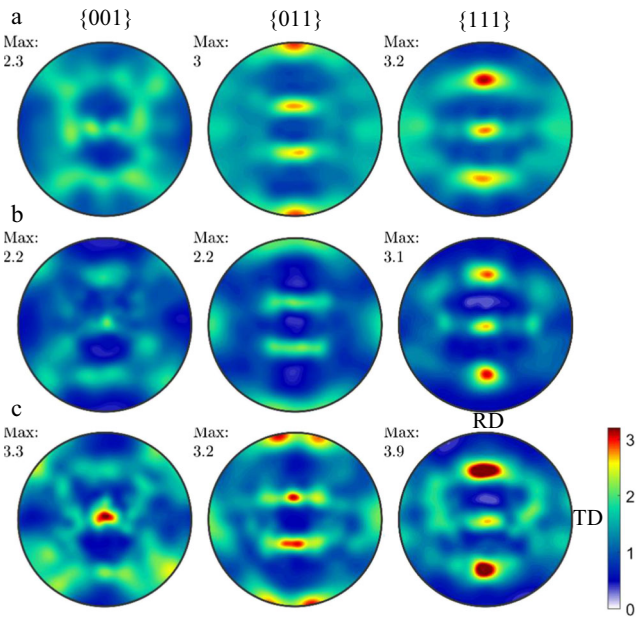

Fig. 10 Stereographic pole figures of DP 1180 measured using the neutron diffraction technique showing texture in the TD **a** initial, **b** after ST away from fracture but within gauge section, and **c** after ST around the fracture zone of the sample

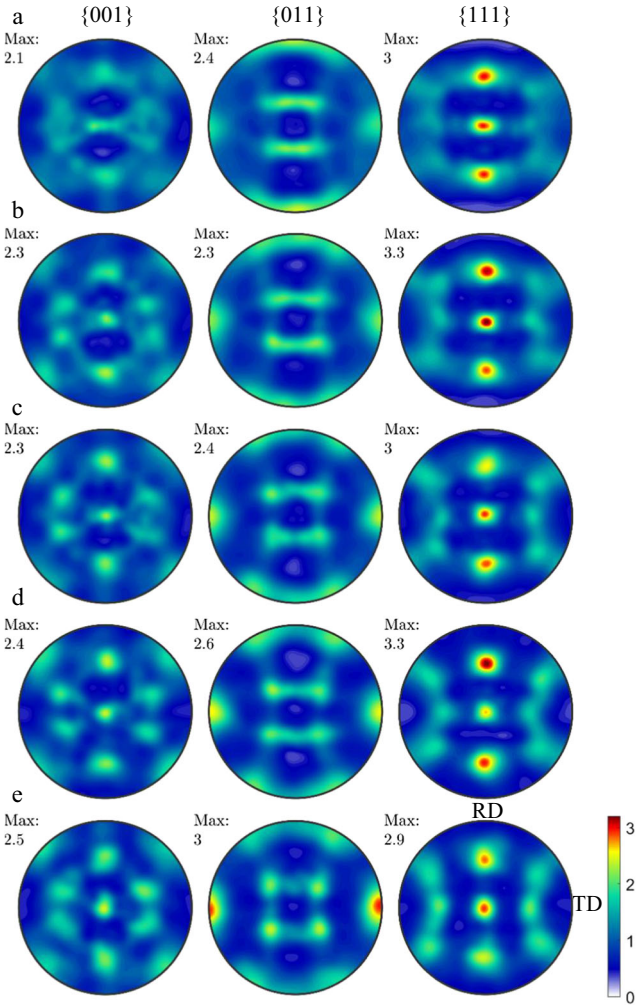

Fig. 11 Stereographic pole figures measured using the neutron diffraction technique showing texture evolution for DP 1180 during CBT along the TD after **a** 2 CBT cycles, **b** 4 CBT cycles **c** 6 CBT cycles, **d** 8 CBT cycles, and **e** 9 CBT cycles at fracture. The CBT testing was performed under 3.5 normalized bend depth and 1.35 mm/s crosshead velocity

because the greatest level of strain is present near the fractured surface. The texture evolution in CBT is shown in Fig. 11. Similar to ST, the {011} poles show the most evolution where the preferred orientation aligns with the TD stretching direction. As is evident, texture in CBT evolves substantially more than in ST. In summary, texture evolution in CBT forms a more pronounced {011} fiber along the stretching direction than in ST, revealing that the deformation in CBT could extend to greater strain levels facilitating more texture evolution than those reached at the fracture location in ST.

Discussion

In this work, the recently built experimental apparatus for CBT of metallic sheets is utilized to evaluate the role of cyclic bending on ETF enhancements for several DP AHSS: DP 590, DP 780, DP

980, and DP 1180. The effect of CBT process parameters (the normalized bend depth and crosshead velocity) in order to maximize the ETF is explored. Results for DP 980 show the remarkable effect of CBT on the ETF and improvement over the results obtained earlier for DP 1180. It is observed that increasing the normalized bend depth and increasing the crosshead velocity increases the ETF, until a peak enhancement is reached. Under a normalized bend depth of 3.5 and crosshead velocity of 1.35 mm/s, ETF of both DP 980 and DP 1180 improves over five times compared to ST for every tested direction. In addition to testing, a combination of electron microscopy along with EBSD and ND is employed in order to assess the initial microstructure, evolution of crystallographic texture, and fracture mechanisms for the studied steels. Texture evolution in CBT forms a more pronounced {011} fiber along the stretching direction than in ST, revealing that the deformation in CBT could extend to greater strain levels than those reached at the fracture location in ST. To the authors' knowledge, this is the largest ever observed change in texture during tension of DP 1180.

The objective of the current work was also to compare the effect of CBT on improved ETF for DP steels as a function of their martensite content and sheet thicknesses. Volume fraction of martensite per steel is estimated to be 7.7% for DP 590, 34% for DP 780, 39% for DP 980, and 45% for DP 1180. To this end, samples of DP 590 and DP 780 were tested under the optimal parameters. The role of thickness comes from the level of applied bending stress/strain, which scales with curvature and sheet thickness. The addition of bending-induced tensile stress to the tensile stress due to stretching is larger for thicker sheets. As a result, a lower force is required to reach the plastic flow stress of the material in the outer surface (top and bottom) of the strip for thicker sheets for a given width (i.e. cross-sectional area). Better behavior in CBT of DP 980 than DP 1180 implies the role of martensite, i.e., the lower the content, the larger ETF effect. The CBT behavior of DP 780 should be enhanced considering the content of martensite. However, the increase in sheet thickness significantly deteriorated the CBT behavior. The effect of thickness and martensitic content is finally verified after testing of DP 590 sheets in CBT. A superior CBT behavior is obtained with DP 590 relative to DP 780 because of the lower content of martensite and the reduced sheet thickness.

One interesting trend to note is the fracture angle of a specimen processed by CBT. Figure 12 shows photographs of fractured specimens in ST and CBT. In ST, DP steels fracture at an oblique angle relative to the stretching direction after necking [78]. However, under CBT testing, all the DP steels fractured at a 90° angle relative to the stretching direction after some amount of necking near fracture, though not as large as in the case of ST. Figure 12 also compares SEM imaging of the fractured edge of DP 1180 specimens fractured in both monotonic ST and CBT. As expected due to necking at the fracture site, both samples show microvoid coalescence, which is an indication of ductile fracture. However, the fracture voids in ST are much coarser. Comparing micrographs in Fig. 12c (ST after interrupting CBT processing to only 2 CBT cycles) and Fig. 12d (ST after interrupting CBT processing to substantial 10 CBT cycles) also indicated that CBT processing is reducing size of the dimples. In general, dimples are known to be finer in size after low cycle fatigue fracture than monotonic ST fracture [79]. Moreover, there also appears to be some brittle fracture through the martensite grains in ST, especially visible in Fig. 12a, c. The insert in Fig. 12c also shows evidence of secondary cracks in martensite forming during plastic deformation. Thus, ductile failure in the ferrite matrix (coarse dimples) are combined with the interfacial fracture with some brittle, flat failure surfaces cutting through martensite grains for ST. Similar findings were also reported in [45] for other high martensite volume fraction DP steels in which the fracture is, like here, influenced by the contrasting phase characteristics and driven by ferrite/martensite interface decohesion and fracture of martensite regions in addition to microvoid coalescence. None of the fractographs show the content of 45% martensite meaning that fracture favors ferrite or interfaces. Considering that the flat surfaces through martensitic grains are primarily seen for the samples fractures in monotonic ST and pre-deformed in CBT followed by ST indicates that fracture in CBT exhibits much more ductile character, which is dependent on existence of fine ductile dimples through ferrite, than fracture in ST. The insert in Fig. 12d shows fracture of a martensite region surrounded by microvoids.

In closing, as CBT has been shown to stretch a ductile sheet metals significantly more than ST, the test can be used to characterize sheet metals at very large strains. Such characterization is useful for the FEM analysis of sheet metal forming operations because many such operations often strain the material beyond the uniform elongation achieved in ST. It is also anticipated that the observations in terms of the improved formability can be utilized in real forming processes of metallic sheets. For example, reciprocating rollers in the binder area or a wavy contour in the forming cavity over which the sheet traverses could be incorporated into drawing processes in order to take advantage of the enhanced elongation observed in CBT processing.

Conclusion

This work presented significant improvements in ETF achieved by imposing bending during stretching using a CBT process for several DP steels. The CBT test incrementally elongates the entire gauge length of the specimen preventing localization of deformation and the necking instability. Remarkably, for an optimized set of CBT parameters, these improvements obtained for 1 mm thick DP 980 and DP 1180 can be over five times greater relative to ST. The other

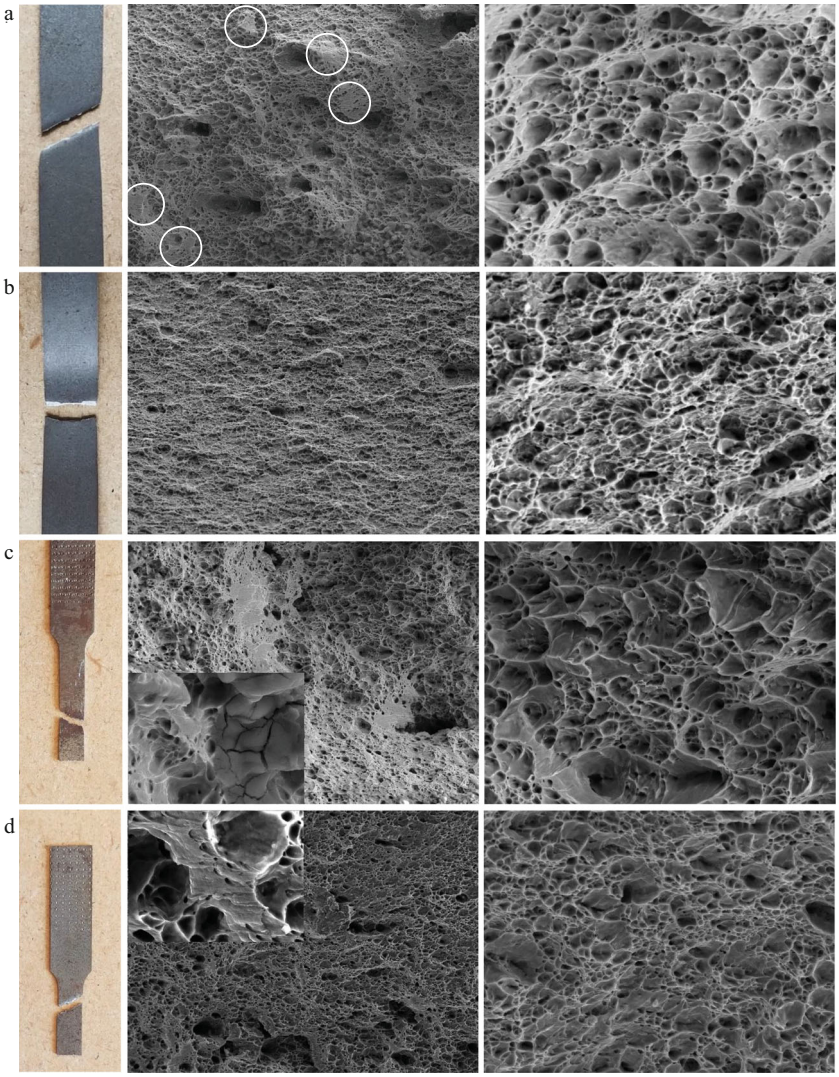

Fig. 12 Fractured samples and SE micrographs showing fractured surfaces of DP 1180 in **a** ST at a strain rate of 10^{-3} s^{-1}, **b** CBT to fracture at 1.35 mm/s crosshead velocity and 3.5 normalized bend depth, **c** ST after interrupting CBT processing at 2 CBT cycles, and **d** ST after interrupting CBT processing at 10 CBT cycles. The samples were tested along RD, while the micrographs are perpendicular to the fracture surface. View field for images on the center is 200 μm in width and 150 μm in height, while those on the right are 50 μm × 40 μm. The inserts in (c) and (d) are 15 μm wide. A few flat failure surfaces cutting through martensite grains are indicated by white circles in (a)

studied AHSS sheets of DP 590 and DP 780 had different thicknesses, in addition to intrinsically containing different fractions of ferrite and martensitic phases. Based on comprehensive data, it is found that lowering of the martensitic content moderately improves ETF, while increasing of the sheet thickness rapidly deteriorates ETF, under CBT. The behavior in tension of sheets that were subjected to CBT processing under the established optimal process conditions has also been investigated, to determine enhancement in strength and any residual ductility of the materials. These secondary ST tests showed that the AHSS exhibited a higher yield stress and decreased elongation relative to the ST response of the as-received material. The strength of the material increased with the number of CBT cycles and the effect was greater in sheets with less martensite. Characterization of texture evolution after CBT testing to certain number of cycles found that texture forms a more pronounced {011} fiber along the stretching direction than in ST. As such, texture evolution is evidence that the deformation in CBT could extend to far greater strain levels than those reached at the fracture location in ST. Fractured surfaces after CBT are found to consist of fine ductile dimples, while those after ST consist of coarser dimples, interfacial fracture, and some content of brittle flat martensitic regions. Thus, even for high martensite containing steels, conventional microvoid coalescence in the ferrite phase can be a prevalent fracture mechanism.

Acknowledgements This research was sponsored by the U.S. National Science Foundation and was accomplished under the CAREER grant no. CMMI-1650641. The authors acknowledge N. C. Ferreri for help with processing of the neutron diffraction data.

Data availability The raw/processed data required to reproduce these findings cannot be shared at this time due to technical or time limitations.

Compliance with ethical standards

Conflict of interest The authors declare that they have no conflict of interest.

Appendix

Table 3 Properties based on the flow curves from Fig. 9

DP 590	Tension	2 cycles	4 cycles	6 cycles	8 cycles	10 cycles	12 cycles
0.2% offset yield stress (MPa)	407	641	665	704	742	1011	1011
UTS (MPa)	663	744	781	816	864	1061	1078
Eng. strain at UTS	0.146	0.0609	0.029	0.0283	0.0253	0.0244	0.0234
Eng. strain at fracture	0.187	0.155	0.111	0.0898	0.07	0.052	0.052
DP 780	Tension	2 cycles	4 cycles	6 cycles	8 cycles	10 cycles	
0.2% offset yield stress (MPa)	528	793	811	895	901	905	
UTS (MPa)	913	1011	1080	1122	1151	1187	
Eng. strain at UTS	0.109	0.02988	0.0266	0.0249	0.0252	0.0248	
Eng. strain at fracture	0.1318	0.1086	0.0675	0.0538	0.0411	0.0369	
DP 980 (RD)	Tension	2 cycles	4 cycles	6 cycles	8 cycles		
0.2% offset yield stress (MPa)	630	849	886	909	944		
UTS (MPa)	987	1102	1165	1192	1242		
Eng. strain at UTS	0.0808	0.0265	0.0262	0.0248	0.027		
Eng. strain at fracture	0.0971	0.0734	0.061	0.044	0.05		
DP 980 (TD)	Tension	2 cycles	4 cycles	6 cycles	8 cycles		
0.2% offset yield stress (MPa)	634	908	956	961	1031		
UTS (MPa)	1012	1134	1190	1224	1257		
Eng. strain at UTS	0.0658	0.030	0.0268	0.0261	0.0232		
Eng. strain at fracture	0.0764	0.0664	0.0472	0.0398	0.0360		
DP 1180 (RD)	Tension	2 cycles	4 cycles	6 cycles	8 cycles	10 cycles	
0.2% offset yield stress (MPa)	839	1197	1311	1354	1382	1454	
UTS (MPa)	1194	1285	1385	1459	1477	1534	
Eng. strain at UTS	0.0619	0.0169	0.0161	0.016	0.0144	0.018	
Eng. strain at fracture	0.0767	0.0626	0.0467	0.0358	0.0267	0.0333	
DP 1180 (TD)	Tension	2 cycles	4 cycles	6 cycles	8 cycles		
0.2% offset yield stress (MPa)	851	1214	1315	1341	1396		
UTS (MPa)	1223	1328	1404	1460	1489		
Eng. strain at UTS	0.0545	0.0169	0.014	0.0137	0.0151		
Eng. strain at fracture	0.064	0.0486	0.0348	0.0295	0.0266		

References

1. Ma B, Liu ZG, Jiang Z, Wu X, Diao K, Wan M (2016) Prediction of forming limit in DP590 steel sheet forming: an extended fracture criterion. Mater Des 96:401–408
2. Hirsch J, Al-Samman T (2013) Superior light metals by texture engineering: optimized aluminum and magnesium alloys for automotive applications. Acta Mater 61:818–843
3. Bhargava M, Chakrabarty S, Barnwal VK, Tewari A, Mishra SK (2018) Effect of microstructure evolution during plastic deformation on the formability of transformation induced plasticity and Quenched & Partitioned AHSS. Mater Des 152:65–77
4. Hirsch J (2014) Recent development in aluminium for automotive applications. Trans Nonferrous Metals Soc China 24:1995–2002
5. Zarei H (2008) Experimental and numerical investigation of crash structures using aluminum alloys. Cuvillier Verlag, Göttingen, Germany
6. Bouaziz O, Zurob H, Huang M (2013) Driving force and logic of development of advanced high strength steels for automotive applications. Steel Res Int 84:937–947
7. Knezevic M, Crapps J, Beyerlein IJ, Coughlin DR, Clarke KD, McCabe RJ (2016) Anisotropic modeling of structural components using embedded crystal plasticity constructive laws within finite elements. Int J Mech Sci 105:227–238
8. Jahedi M, McWilliams BA, Moy P, Knezevic M (2017) Deformation twinning in rolled WE43-T5 rare earth magnesium alloy: influence on strain hardening and texture evolution. Acta Mater 131:221–232

9. Zecevic M, Knezevic M (2018) A new visco-plastic self-consistent formulation implicit in dislocation-based hardening within implicit finite elements: application to high strain rate and impact deformation of tantalum. Comput Methods Appl Mech Eng 341:888–916
10. Ardeljan M, Knezevic M (2018) Explicit modeling of double twinning in AZ31 using crystal plasticity finite elements for predicting the mechanical fields for twin variant selection and fracture analyses. Acta Mater 157:339–354
11. Zecevic M, Knezevic M (2018) Latent hardening within the elasto-plastic self-consistent polycrystal homogenization to enable the prediction of anisotropy of AA6022-T4 sheets. Int J Plast 105:141–163
12. Zecevic M, Knezevic M (2017) Modeling of sheet metal forming based on implicit embedding of the Elasto-plastic self-consistent formulation in Shell elements: application to cup drawing of AA6022-T4. JOM 69:922–929
13. Zecevic M, Knezevic M (2019) An implicit formulation of the elasto-plastic self-consistent polycrystal plasticity model and its implementation in implicit finite elements. Mech Mater 136:103065
14. Zecevic M, Beyerlein IJ, Knezevic M (2017) Coupling elasto-plastic self-consistent crystal plasticity and implicit finite elements: applications to compression, cyclic tension-compression, and bending to large strains. Int J Plast 93:187–211
15. Music O, Allwood J, Kawai K (2010) A review of the mechanics of metal spinning. J Mater Process Technol 210:3–23
16. Quigley E, Monaghan J (2000) Metal forming: an analysis of spinning processes. J Mater Process Technol 103:114–119
17. Wang L, Long H (2011) Investigation of material deformation in multi-pass conventional metal spinning. Mater Des 32:2891–2899
18. Emmens WC, van den Boogaard AH (2009) An overview of stabilizing deformation mechanisms in incremental sheet forming. J Mater Process Technol 209:3688–3695
19. Eyckens P, Van Bael A, Van Houtte P (2009) Marciniak–Kuczynski type modelling of the effect of through-thickness shear on the forming limits of sheet metal. Int J Plast 25:2249–2268
20. Allwood JM, Shouler DR (2009) Generalised forming limit diagrams showing increased forming limits with non-planar stress states. Int J Plast 25:1207–1230
21. Yagami T, Manabe K, Miyamoto T (2009) Ductile fracture behavior of 5052 aluminum alloy sheet under cyclic plastic deformation at room temperature. J Mater Process Technol 209:1042–1047
22. Swift H (1948) Plastic bending under tension. Engineering 166: 333–359
23. Benedyk J, Parikh N, Stawarz D (1971) A method for increasing elongation values for ferrous and nonferrous sheet metals. J Mater 6:16–29
24. Schleich R, Held C, Sindel M, Liewald M (2009) Investigation on the effect of curvature and sheet thickness on forming limit prediction for aluminium sheet metal alloys. Int J Mater Form 2:411
25. Nine H (1978) Drawbead forces in sheet metal forming. Mechanics of Sheet Metal Forming. Springer, Boston, pp 179–211
26. Zecevic M, Roemer T, Knezevic M, Korkolis Y, Kinsey B (2016) Residual ductility and microstructural evolution in continuous-bending-under-tension of AA-6022-T4. Materials 9:130
27. Emmens WC, van den Boogaard AH (2009) Incremental forming by continuous bending under tension—an experimental investigation. J Mater Process Technol 209:5456–5463
28. Calcagnotto M, Ponge D, Raabe D (2012) Microstructure control during fabrication of ultrafine grained dual-phase steel: characterization and effect of intercritical annealing parameters. ISIJ Int 52: 874–883
29. Woo W, Em VT, Kim EY, Han SH, Han YS, Choi SH (2012) Stress–strain relationship between ferrite and martensite in a dual-phase steel studied by in situ neutron diffraction and crystal plasticity theories. Acta Mater 60:6972–6981
30. Gong H, Wang S, Knysh P, Korkolis YP (2016) Experimental investigation of the mechanical response of laser-welded dissimilar blanks from advanced- and ultra-high-strength steels. Mater Des 90:1115–1123
31. Ghaei A, Green DE, Aryanpour A (2015) Springback simulation of advanced high strength steels considering nonlinear elastic unloading–reloading behavior. Mater Des 88:461–470
32. Zecevic M, Upadhyay MV, Polatidis E, Panzner T, Van Swygenhoven H, Knezevic M (2019) A crystallographic extension to the Olson-Cohen model for predicting strain path dependence of martensitic transformation. Acta Mater 166:386–401
33. Kudzal AD, McWilliams BA, Taggart-Scarff J, Knezevic M (2020) Fabrication of a low alloy ultra-high strength (>1500 MPa yield) steel using powder bed fusion additive manufacturing. Mater Sci Eng A 770:138512
34. Calcagnotto M, Adachi Y, Ponge D, Raabe D (2011) Deformation and fracture mechanisms in fine- and ultrafine-grained ferrite/martensite dual-phase steels and the effect of aging. Acta Mater 59:658–670
35. Tasan CC, Hoefnagels JPM, Diehl M, Yan D, Roters F, Raabe D (2014) Strain localization and damage in dual phase steels investigated by coupled in-situ deformation experiments and crystal plasticity simulations. Int J Plast 63:198–210
36. Kapp M, Hebesberger T, Kolednik O (2011) A micro-level strain analysis of a high-strength dual-phase steel. Int J Mater Res 102: 687–691
37. Eghtesad A, Knezevic M (2020) High-performance full-field crystal plasticity with dislocation-based hardening and slip system back-stress laws: application to modeling deformation of dual-phase steels. J Mech Phys Solids 134:103750
38. Wagoner RH, Kim JH, Sung JH (2009) Formability of advanced high strength steels. Int J Mater Form 2:359
39. Bhadeshia HKDH (2002) TRIP-assisted steels? ISIJ Int 42:1059–1060
40. Shi M, Gelisse S (2006) Issues on the AHSS forming limit determination. Proceedings of the IDDRG International Conference, Porto, pp 19–21
41. Nikhare C, Hodgson P, Weiss M (2011) Necking and fracture of advanced high strength steels. Mater Sci Eng A 528:3010–3013
42. Saeidi N, Ashrafizadeh F, Niroumand B, Barlat F (2015) EBSD study of micromechanisms involved in high deformation ability of DP steels. Mater Des 87:130–137
43. Xue X, Liao J, Vincze G, Sousa J, Barlat F, Gracio J (2016) Modelling and sensitivity analysis of twist springback in deep drawing of dual-phase steel. Mater Des 90:204–217
44. Barrett TJ, Knezevic M (2019) Deep drawing simulations using the finite element method embedding a multi-level crystal plasticity constitutive law: experimental verification and sensitivity analysis. Comput Methods Appl Mech Eng 354:245–270
45. Sun X, Choi KS, Soulami A, Liu WN, Khaleel MA (2009) On key factors influencing ductile fractures of dual phase (DP) steels. Mater Sci Eng A 526:140–149
46. Sun X, Choi KS, Liu WN, Khaleel MA (2009) Predicting failure modes and ductility of dual phase steels using plastic strain localization. Int J Plast 25:1888–1909
47. Gribbin S, Bicknell J, Jorgensen L, Tsukrov I, Knezevic M (2016) Low cycle fatigue behavior of direct metal laser sintered Inconel alloy 718. Int J Fatigue 93(Part 1):156–167
48. Gribbin S, Ghorbanpour S, Ferreri NC, Bicknell J, Tsukrov I, Knezevic M (2019) Role of grain structure, grain boundaries, crystallographic texture, precipitates, and porosity on fatigue behavior of Inconel 718 at room and elevated temperatures. Mater Charact 149:184–197
49. Smith DH, Bicknell J, Jorgensen L, Patterson BM, Cordes NL, Tsukrov I, Knezevic M (2016) Microstructure and mechanical behavior of direct metal laser sintered Inconel alloy 718. Mater Charact 113:1–9

50. Ghorbanpour S, McWilliams BA, Knezevic M (2019) Effect of hot working and aging heat treatments on monotonic, cyclic, and fatigue behavior of WE43 magnesium alloy. Mater Sci Eng A 747:27–41
51. Ghorbanpour S, Zecevic M, Kumar A, Jahedi M, Bicknell J, Jorgensen L, Beyerlein IJ, Knezevic M (2017) A crystal plasticity model incorporating the effects of precipitates in superalloys: application to tensile, compressive, and cyclic deformation of Inconel 718. Int J Plast 99:162–185
52. Poulin CM, Korkolis YP, Kinsey BL, Knezevic M (2019) Over five-times improved elongation-to-fracture of dual-phase 1180 steel by continuous-bending-under-tension. Mater Des 161:95–105
53. Cantara AM, Zecevic M, Eghtesad A, Poulin CM, Knezevic M (2019) Predicting elastic anisotropy of dual-phase steels based on crystal mechanics and microstructure. Int J Mech Sci 151:639–649
54. Zecevic M, Korkolis YP, Kuwabara T, Knezevic M (2016) Dual-phase steel sheets under cyclic tension–compression to large strains: experiments and crystal plasticity modeling. J Mech Phys Solids 96:65–87
55. Holscher M, Raabe D, Lucke K (1994) Relationship between rolling textures and shear textures in F.C.C. and B.C.C. metals. Acta Metall Mater 42:879–886
56. Kocks UF, Tomé CN, Wenk H-R (1998) Texture and anisotropy. Cambridge University Press, Cambridge
57. Bhattacharyya A, Knezevic M, Abouaf M (2015) Characterization of crystallographic texture and intra-grain morphology in cross-rolled tantalum. Metall Mater Trans A 46:1085–1096
58. Knezevic M, Zecevic M, Beyerlein IJ, Bhattacharyya A, McCabe RJ (2015) Predicting texture evolution in ta and ta-10W alloys using Polycrystal plasticity. JOM 67:2670–2674
59. Knezevic M, Beyerlein IJ, Lovato ML, Tomé CN, Richards AW, McCabe RJ (2014) A strain-rate and temperature dependent constitutive model for BCC metals incorporating non-Schmid effects: application to tantalum–tungsten alloys. Int J Plast 62:93–104
60. Knezevic M, Bhattacharyya A (2017) Characterization of microstructure in Nb rods processed by rolling: effect of grooved rolling die geometry on texture uniformity. Int J Refract Met Hard Mater 66:44–51
61. Knezevic M, Nizolek T, Ardeljan M, Beyerlein IJ, Mara NA, Pollock TM (2014) Texture evolution in two-phase Zr/Nb lamellar composites during accumulative roll bonding. Int J Plast 57:16–28
62. Knezevic M, Landry NW (2015) Procedures for reducing large datasets of crystal orientations using generalized spherical harmonics. Mech Mater 88:73–86
63. Barrett TJ, Eghtesad A, McCabe RJ, Clausen B, Brown DW, Vogel SC, Knezevic M (2019) A generalized spherical harmonics-based procedure for the interpolation of partial datasets of orientation distributions to enable crystal mechanics-based simulations. Materialia 6:100328
64. Zecevic M, Knezevic M, Beyerlein IJ, Tomé CN (2015) An elasto-plastic self-consistent model with hardening based on dislocation density, twinning and de-twinning: application to strain path changes in HCP metals. Mater Sci Eng A 638:262–274
65. Knezevic M, Beyerlein IJ, Brown DW, Sisneros TA, Tomé CN (2013) A polycrystal plasticity model for predicting mechanical response and texture evolution during strain-path changes: application to beryllium. Int J Plast 49:185–198
66. Feather WG, Ghorbanpour S, Savage DJ, Ardeljan M, Jahedi M, McWilliams BA, Gupta N, Xiang C, Vogel SC, Knezevic M (2019) Mechanical response, twinning, and texture evolution of WE43 magnesium-rare earth alloy as a function of strain rate: experiments and multi-level crystal plasticity modeling. Int J Plast 120:180–204
67. Ardeljan M, Beyerlein IJ, McWilliams BA, Knezevic M (2016) Strain rate and temperature sensitive multi-level crystal plasticity model for large plastic deformation behavior: application to AZ31 magnesium alloy. Int J Plast 83:90–109
68. Benedyk DSJC, Parikh NM (1971) A method for increasing elongation values for ferrous and nonferrous sheet metals. J Mater
69. Emmens WC, van den Boogaard AH (2011) Cyclic stretch-bending: mechanics, stability and formability. J Mater Process Technol 211:1965–1981
70. Roemer TJ, Barrett TJ, Knezevic M, Kinsey BL, Korkolis YP (2019) Experimental study of continuous-bending-under-tension of AA6022-T4. J Mater Process Technol 266:707–714
71. Emmens WC, Sebastiani G, van den Boogaard AH (2010) The technology of incremental sheet forming—a brief review of the history. J Mater Process Technol 210:981–997
72. Allwood JM, Shouler DR, Tekkaya AE (2007) The increased forming limits of incremental sheet forming processes. Key Eng Mater 344:621–628
73. Y. Huang, J. Cao, K. Smith, B. Woody, J. Ziegert, M. Li. Experimental and numerical investigation of forming limits in incremental forming of a conical cup. Transactions of the North American Manufacturing Research Institution of SME, 2008
74. Knezevic M, Poulin CM, Zheng X, Zheng S, Beyerlein IJ (2019) Strengthening of alloy AA6022-T4 by continuous bending under tension. Mater Sci Eng A 758:47–55
75. Wenk H-R, Lutterotti L, Vogel S (2003) Texture analysis with the new HIPPO TOF diffractometer. Nucl Instrum Meth A 515:575–588
76. Wenk H-R, Lutterotti L, Vogel S (2010) Rietveld texture analysis from TOF neutron diffraction data. Powder Diffract 25:283–296
77. Bachmann F, Hielscher R, Schaeben H (2010) Texture analysis with MTEX–free and open source software toolbox. Solid State Phenom 160:63–68
78. Hosford WF, Caddell RM (2011) Metal forming: mechanics and metallurgy. Cambridge University Press, New York
79. Ghorbanpour S, McWilliams BA, Knezevic M (2019) Low-cycle fatigue behavior of rolled WE43-T5 magnesium alloy. Fatigue Fract Eng Mater Struct 42:1357–1372